FoMR
Frontiers of Multidisciplinary Research

Vol. 1 | No. 4 | Oct - Dec 2026

Microwave-Assisted Green Synthesis and Temperature-Dependent Dielectric Relaxation of Nominal $MgFe_{2-x}Ni_xO_4$ Spinel Ferrites Using Tinospora cordifolia

Shivshankar Prasad Pandey[a*], Tiwari K.P[b*], Tewari H.S[c*]

ABSTRACT

Nominal $MgFe_{2-x}Ni_xO_4$ spinel ferrites (x = 0.05, 0.10, 0.15 and 0.20) were prepared by a microwave-assisted green combustion route using Tinospora cordifolia stem extract as a natural complexing/combustion medium. The precursor solution was subjected to 2.45 GHz and 600 W for approximately 5 min and used without a separate post-combustion calcination step. X-ray diffraction patterns indicated the presence of a cubic spinel structure. Crystallite-size estimates obtained using the Scherrer, Williamson-Hall and size-strain plot methods gave values of 15.87–17.82, 21.69–26.07 and 18.81–21.76 nm, respectively. The differences among the three methods reflect the contributions of crystallite-size and lattice-strain broadening. The lattice parameter was narrowly dispersed between 8.37083 and 8.38871 Å. Pellets sintered at 600 °C for 4 h had bulk densities of 3.95–4.08 $g.cm^{-3}$ and apparent porosities of 9.79-12.66%. Dielectric measurements from 1 Hz to 100 kHz and room temperature to 400 °C showed strong frequency dispersion and a marked suppression of 1 kHz low-temperature dielectric constant from 111.42 at x = 0.05 to 14.326 at x = 0.20. Broadened, frequency-dependent maxima of M″ showed a thermal shift, reflecting distributed thermally activated relaxation. Arrhenius analysis of M″ maxima provided values of effective activation energy as 0.779 eV for x = 0.05, 0.484 eV for x = 0.10, 0.480 eV for x = 0.15 and 0.662 eV for x = 0.20. The R^2 value for x = 0.20 was lower (0.849); therefore, this result should be interpreted with caution. The findings show that nominal Ni-for-Fe substitution combined with microwave-assisted synthesis using plant material can modify the electrical characteristics of the ferrite series.

Received date: 30.08.2026
Accepted date: 12.10.2026

Keywords: Magnetic ceramics, Ferrites, Dielectric properties, Microwave processing

https://doi.org/10.65601/FoMR.2026.1.4.1

***Corresponding Authors:**

[a]*Government E R R Science P G College, Bilaspur, Chhattisgarh, India*
email: shivpandeybsp@gmail.com

[b]*Government E R R Science P G College, Bilaspur, Chhattisgarh, India*

[c]*Department of Pure & Applied Physics, Guru Ghasidas University, Bilaspur, Chhattisgarh, India*

All the articles published in FoMR are open-access, providing free access to everyone. FoMR articles are licensed under the Creative Commons Attribution licence (https://creativecommons.org/share-your-work/cclicenses/). This license enables reusers to distribute, remix, adapt, and build upon the material in any medium or format, so long as attribution is given to the creator. The license allows for commercial use.

INTRODUCTION

The spinel-type ferrites represented by the composition formula AB_2O_4 have been considered an important class of oxide ceramic materials in technology due to the influence of cation arrangement in tetrahedral and octahedral sublattices on their structure, magnetism and electric properties. The chemical stability, relatively high resistivity and adjustable dielectric properties have enabled their use in high frequency devices, electromagnetic devices, sensors and other energy-related applications (Dippong et al., 2021; Sickafus et al., 1999). Magnesium ferrite ($MgFe_2O_4$) is an inverse-spinel compound, the functionality of which is highly dependent on preparation method, thermal treatment, defects and cation rearrangement (Araújo et al., 2021; Tahir et al., 2024). Nickel incorporation is an established strategy for modifying magnesium-ferrite properties. Importantly, $MgFe_{2-x}Ni_xO_4$ (MFNO) compositions in the low-Ni range have been reported previously: Tadi et al. (2010) studied x = 0.01-0.20 after high-temperature annealing and found composition-dependent structural, magnetic and dielectric behavior. The related XRD/XPS study on the topic of Mg-Ni ferrites further proves that the cation distribution and oxidation state need to be taken into consideration when analyzing the nominal composition (Mittal et al., 2004). The more recent studies conducted for $MgFe_2O_4$ ferrite containing Ni and Mg-Ni ferrites have proved once again that the electrical characteristics of such materials can be modified by cation substitution and thermal treatment (Bouzidi et al., 2025; Dhahri et al., 2025; Hamdaoui et al., 2019; Revathi et al., 2024; Singh et al., 2026). Thus, the nominal composition, in this case, means MFNO; the data obtained with X-ray diffraction (XRD) and energy-dispersive X-ray spectroscopy (EDS) help to identify the phase/elemental dependence but cannot provide information regarding Ni oxidation state and cation sites occupation. Another design parameter is the method of the synthesis. The conventional methods such as ceramic or sol-gel routes are characterized by long heating schedule or calcination process after synthesis, while microwave-assisted combustion allows for fast volumetric heating and quick reactions. Plant extracts offer an additional green-processing advantage because polyphenols, sugars, organic acids and related phytochemicals can coordinate metal ions and promote combustion (Ali et al., 2024; Suresh Kumar et al., 2021). Mg- and Ni-based ferrites via Microwave-assisted green synthesis have already been proven using fuels derived from plants (Suresh Kumar et al., 2021; Vishnu et al., 2023). The plant species Tinospora cordifolia is specifically interesting for being a natural medium for the preparation of the metal oxides since the phytochemicals contained in the stem of Tinospora cordifolia can take part in the complexation and combustion/reduction reactions (Udayabhanu et al., 2015). Despite this progress, the combination of a Tinospora cordifolia-assisted microwave combustion route with the exact low-Ni nominal MFNO series and a broad temperature-dependent dielectric/modulus study remains underexplored. The present study therefore investigates x = 0.05–0.20 powders produced by a ~5 min, 600 W microwave process without a separate powder-calcination step. Structure is cross-examined by Scherrer, Williamson-Hall (W-H) and size-strain plot (SSP) analyses, while Fourier-transform infrared spectroscopy (FTIR), scanning electron microscopy (SEM), and EDS provide complementary bonding, morphology and elemental information. For the electrical study, only the compacted pellets are subsequently sintered at 600 °C for 4 h to obtain mechanically stable electrodes. Dielectric permittivity, loss, alternating-current (AC) conductivity and electric modulus are then followed from room temperature to 400 °C and across 1 Hz-100 kHz. This combined processing-structure-electrical analysis is intended to clarify how low-level nominal Ni-for-Fe substitution modifies polarization and thermally activated relaxation while retaining an energy-efficient powder synthesis route.

EXPERIMENTAL PROCEDURE

Materials and Tinospora cordifolia Extract

Analytical-reagent (AR) grade magnesium nitrate hexahydrate [$Mg(NO_3)_2{\cdot}6H_2O$], ferric nitrate nonahydrate [$Fe(NO_3)_3{\cdot}9H_2O$], and nickel nitrate hexahydrate [$Ni(NO_3)_2{\cdot}6H_2O$], all with purity >98%, were obtained from Qualigens Fine Chemicals, India, and used without further purification. Deionized water was used for extract preparation and precursor processing.

Microwave-Assisted Green Synthesis

Stoichiometric amounts of magnesium nitrate, ferric nitrate and nickel nitrate corresponding to the nominal compositions MFNO (x = 0.05, 0.10, 0.15 and 0.20) were dissolved in the Tinospora cordifolia

extract under constant magnetic stirring. The plant-derived organic constituents acted as complexing species and combustion promoters. The solution was transferred to a borosilicate reaction vessel and irradiated in a domestic microwave oven at 2.45 GHz and 600 W. Within approximately 5 min, rapid dehydration was followed by self-combustion, producing a voluminous porous solid. The as-combusted product was gently ground in an agate mortar. No separate post-combustion calcination was applied to the nanopowder used for structural, FTIR and microstructural characterization.

Structural and Microstructural Characterization

X-ray diffraction (XRD) measurements were carried out on a Rigaku Ultima IV diffractometer using Cu Kα radiation (λ = 1.5406 Å). Data were collected in a 2θ range from 10° to 90° with a step of 0.02°. In order to improve clarity of the main spinel reflections, only the 25–65° section of the recorded patterns is presented in Figure 1. The average crystallite size was first estimated using the Debye–Scherrer relation (Eq. 1), as reported by Manna et al. (2016).

$$D = \frac{K\lambda}{\beta\cos\theta} \tag{1}$$

where D is the average crystallite size, K is the shape factor (0.94), λ is the wavelength of Cu Kα radiation, β is the full width at half maximum (FWHM) of the diffraction peak in radians, and θ is the Bragg angle. To distinguish the contributions of crystallite size and lattice strain to the observed peak broadening, the Williamson–Hall (W–H) method (Eq. 2) was applied using the uniform deformation model (Eq. 3), as reported by Pramanik et al. (2013).

$$\beta\cos\theta = \frac{K\lambda}{\mathrm{D}} + 4\varepsilon\sin\theta \tag{2}$$

where ε represents the lattice microstrain, while K, λ, D, β and θ retain the definitions given above.

$$(\mathrm{d}\beta\cos\theta)^2 = \frac{K\lambda}{\mathrm{D}}(\mathrm{d}^2\beta\cos\theta) + \left(\frac{\varepsilon}{2}\right)^2 \tag{3}$$

where d is the interplanar spacing, and K, λ, D, β and θ retain the definitions given above. The interplanar spacing was determined from Bragg's law (Eq. 4):

$$\mathrm{n}\lambda = 2d\sin\theta \tag{4}$$

where n is the diffraction order, λ is the X-ray wavelength, d is the interplanar spacing and θ is the Bragg angle. For the cubic spinel structure, the lattice parameter was calculated using Eq. 5:

$$a = \frac{d}{(h^2 + k^2 + l^2)^{\frac{1}{2}}} \tag{5}$$

where a is the cubic lattice parameter and h, k and l are the Miller indices.

The theoretical X-ray density (ρ_x) was calculated using Eq. 6, where Z is the number of formula units per unit cell (Z=8 for the cubic spinel structure), M is the molar mass, N_A is Avogadro's constant, and a is the cubic lattice parameter.

$$\rho_x = \frac{ZM}{\mathrm{N}_A\mathrm{a}^3} \tag{6}$$

FTIR spectra were recorded over 400–4000 cm^{-1}. Surface morphology was examined by SEM, and elemental composition was assessed using the attached EDS detector. SEM measurements were performed at an accelerating voltage of 15.0 kV and a working distance of 8.5 mm; representative micrographs were recorded at approximately 3.20 kX magnification with a 10 μm scale bar.

Pellet Preparation and Densification

The as-combusted powders were compacted into circular pellets under an applied load of approximately 5 tonnes using a hydraulic press. The nominal diameter was 13.0 mm; measured thickness and mass varied slightly with composition (Table 2). To improve mechanical stability for dielectric measurements, the green pellets were sintered at 600 °C for 4 h and then cooled naturally to room temperature inside the switched-off furnace. Both pellet faces were coated with silver paste. Electrode area and pellet volume were calculated using $A = \pi r^2$ and $Vp = \pi r^2 t$, respectively, where r is the pellet radius, A is the electrode area, Vp is the pellet volume, and t is the pellet thickness. Bulk density was evaluated from $\rho_b = m/Vp$, where ρ_b is the bulk density and m is the pellet mass, and apparent porosity from $P = (1 - \rho_b/\rho_x) \times 100$, where P is the apparent porosity and ρ_x is the theoretical X-ray density.

Dielectric, Conductivity and Modulus Measurements

Electrical measurements were carried out using

a Hioki inductance-capacitance-resistance (LCR) meter equipped with a Hioki 9140-10 test fixture over 1 Hz–100 kHz from room temperature to 400 °C, with a nominal heating interval of 5 °C. The real part of the dielectric permittivity (ε′), imaginary part of the dielectric permittivity (ε″), alternating-current (AC) conductivity (σ_{ac}), and the real and imaginary parts of the electric modulus (M′ and M″) were calculated using Eqs. (7)–(11), respectively.

$$\varepsilon' = \frac{C_P t}{\varepsilon_0 A} \quad (7)$$

$$\varepsilon'' = \varepsilon' \tan\delta \quad (8)$$

$$\sigma ac = 2\pi f \varepsilon_0 \varepsilon'' \quad (9)$$

$$M' = \frac{\varepsilon'}{(\varepsilon'^2 + \varepsilon''^2)} \quad (10)$$

$$M'' = \frac{\varepsilon''}{(\varepsilon'^2 + \varepsilon''^2)} \quad (11)$$

where C_P is the measured capacitance, t is the pellet thickness, A is the electrode area, ε_0 is the permittivity of free space, f is the applied frequency, tanδ is the dielectric loss tangent, σ_{ac} is the AC conductivity, and M′ and M″ are the real and imaginary parts of the electric modulus, respectively. Conductivity, as calculated using Eq. (12), is reported in S.cm^{-1} after the appropriate conversion of length units.

$$\tau = \frac{1}{2\pi f} \quad (12)$$

where τ is the relaxation time and f is the frequency corresponding to the selected M″ maximum. The temperature dependence of the relaxation time was analyzed using the Arrhenius relation. In Eq. (13), τ_0 is the pre-exponential relaxation time, E_a is the activation energy, k_B is the Boltzmann constant, and T is the absolute temperature in kelvin. The activation energy was obtained from the slope of the linear fit of $\log_{10}\tau$ versus 1000/T.

$$\tau = \tau_0 \exp\frac{E_a}{k_B T} \quad (13)$$

Although the measurements covered the complete **1 Hz–100 kHz** frequency range, the Arrhenius analysis was performed using the four explicitly selected relaxation maxima at **100 Hz, 1 kHz, 10 kHz, and 100 kHz** for each composition, consistent with the peak-selection data presented in the manuscript.

RESULTS AND DISCUSSION

Crystal Structure and Line-Profile Analysis

The XRD patterns of the sample shown in Figure 1 reveals the typical spinel reflections of (220), (311), (400), (511) and (440) planes for the chosen 25–65° range. The observed reflection pattern can be well assigned to a cubic $MgFe_2O_4$-type spinel structure. However, no strong extra peaks are seen in the given XRD pattern within the scan range. By not performing a Rietveld type analysis or quantitative phase analysis, we have described the pattern as being consistent with a major spinel phase, but not necessarily excluding other possible phases. Similarly, such caution is applied to the nominal MFNO since conventional XRD analysis cannot provide information about the oxidation state of Ni and its distribution within the crystal lattice. In particular, the preparation of ceramics with low Ni content at even higher temperatures than those used in this study may lead to cation redistribution affecting the dielectric properties of the material (Mittal et al., 2004; Tadi et al., 2010)

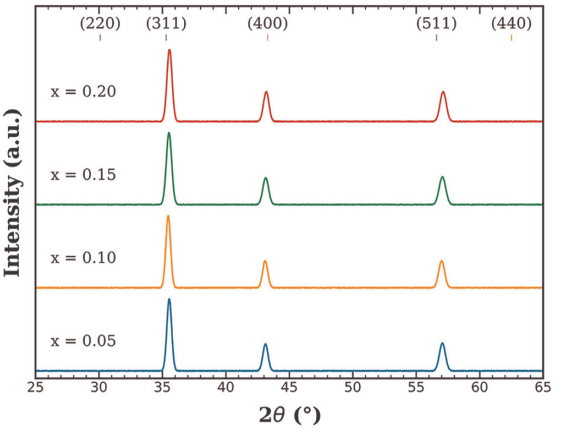


Figure 1 XRD patterns of nominal MFNO (x = 0.05, 0.10, 0.15 and 0.20). Diffraction data were acquired over 2θ = 10–90° with a 0.02° step; only the 25–65° region is displayed to improve visibility of the principal spinel reflections.

The lattice parameter is subject to only minor variations as a function of nominal Ni content, ranging from 8.37871 Å (x = 0.05) up to a maximum of 8.38871 Å (x = 0.10) and subsequently decreases to 8.37083 Å at x = 0.20 (Table 1). The unit-cell volume follows an analogous small non-monotonic trend. Such small variations indicate that the accommodation of the substitution is mostly realized by local cation/defect rearrangements

without a significant volume expansion/contraction of the spinel framework. A similar sensitivity of the Mg-ferrite lattice and dielectric behavior to cation chemistry was observed for several substituted systems (Araújo et al., 2021; Batoo et al., 2017; Revathi et al., 2024; Srimathi et al., 2025).

Table 1 Structural parameters and crystallite-size estimates for nominal MFNO.

x	a (Å)	V (Å³)	Scherrer D (nm)	W-H D (nm)	SSP D (nm)	ρx (g.cm-3)
0.05	8.37871	588.2087	17.56	26.07	21.75	4.5199
0.10	8.38871	590.3173	17.82	25.59	21.76	4.5069
0.15	8.37899	588.2677	15.87	21.69	18.81	4.5259
0.20	8.37083	586.5507	16.76	22.47	19.64	4.5423

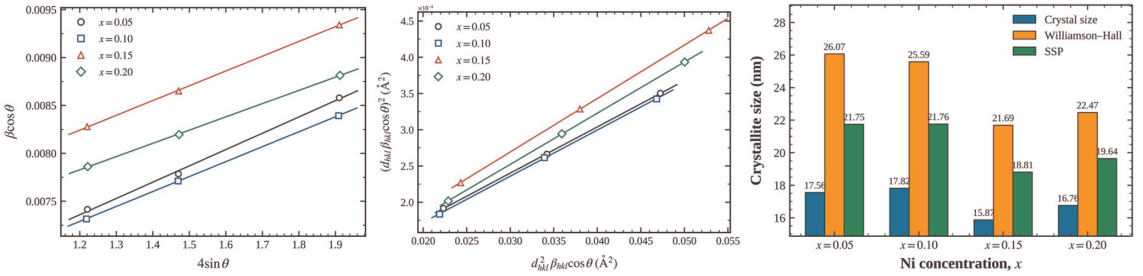


Figure 2 XRD line-profile analysis of MFNO: (a) W-H plots, (b) SSP and (c) comparison of crystallite sizes obtained by Scherrer, W-H and SSP methods.

On the basis of three line-broadening approaches, the absolute crystallite sizes obtained demonstrate a systematically different trend, but a consistent composition-sensitive behavior (Figure 2). The Scherrer values are 17.56, 17.82, 15.87 and 16.76 nm for x = 0.05, 0.10, 0.15 and 0.20, while the W-H values (26.07, 25.59, 21.69 and 22.47 nm) are bigger than the SSP estimations (21.75, 21.76, 18.81 and 19.64 nm) which are placed in the middle of former and latter values. The minimum was found at x = 0.15 in all three analyses followed by the partial recovery at x = 0.20. The discrepancy in the cross-method comparison can be explained due to the fact that the Scherrer equation attributes all peak broadening to the finite size effects, while the strain aware approaches explicitly separate the size and strain contributions. In such a way, the agreement in the composition trend on the basis of three methods appears to be more informative than any individual analysis.

The theoretical X-ray density remains near 4.51–4.54 g.cm^{-3} (Table 1). Using the independently measured pellet geometry, the sintered bulk density

Table 2 Pellet geometry, bulk density and apparent porosity after sintering at 600 °C for 4 h.

x	Diameter (mm)	Thickness (mm)	Mass (g)	Volume (cm³)	ρ_b (g.cm-3)	Porosity (%)
0.05	13.0	1.50	0.786	0.19910	3.9478	12.66
0.10	13.0	1.48	0.795	0.19644	4.0470	10.21
0.15	13.0	1.48	0.802	0.19644	4.0826	9.79
0.20	13.0	1.49	0.806	0.19777	4.0754	10.28

rises from 3.948 g.cm^{-3} at x = 0.05 to approximately 4.08 g.cm^{-3} at x = 0.15-0.20, while apparent porosity falls from 12.66% to a minimum of 9.79% at x = 0.15 before increasing slightly to 10.28% at x = 0.20 (Table 2). The densification trend is therefore non-monotonic and should not be reduced to a simple increase with Ni content.

FTIR Response

The stacked FTIR spectra (Figure 3) show the strong low-wavenumber absorption characteristic of metal-oxygen vibrations in spinel ferrites. In cubic ferrites, the higher-frequency metal-oxygen band is generally associated with tetrahedral coordination and the lower-frequency band with octahedral coordination (Srinivasan et al., 1984). The present spectra also contain weaker features at higher wavenumber that may arise from adsorbed water, hydroxyl groups or residual surface species from the plant-assisted combustion process. Because no peak-fitting table or complementary Raman/XPS measurement was supplied, small band shifts are not over-interpreted as proof of a specific Ni site occupancy.

Morphology and Elemental Composition

The SEM micrographs (Figure 4) show irregular, agglomerated and locally porous clusters for all compositions. Such morphology is to be expected from fast microwave combustion where a sudden gas evolution may generate a low density, foamy like precursor product prior the pelletizing step. Similar sponge-like agglomerates have been reported for microwave/plant assisted ferrite synthesis (Suresh Kumar et al., 2021; Vishnu et al., 2023). Note that the SEM scale is 10 µm which means that the

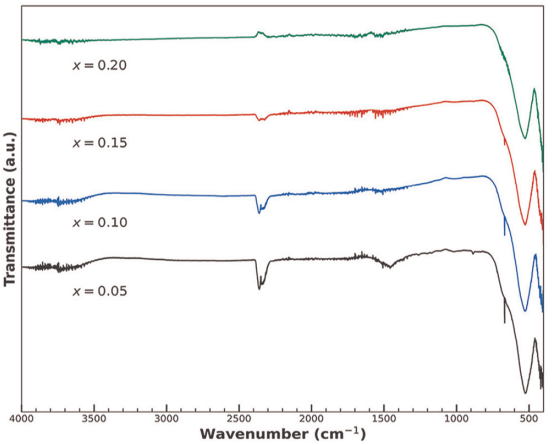


Figure 3 FTIR spectra of nominal MFNO (x = 0.05–0.20) recorded over 400–4000 cm-1.

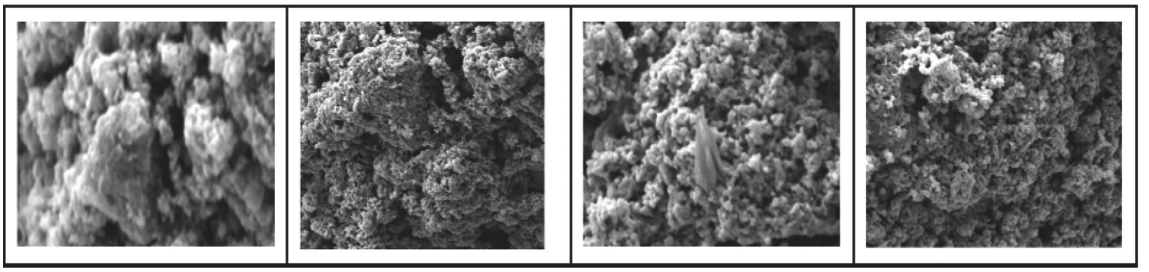


Figure 4 SEM micrographs of nominal MFNO: (a) x = 0.05, (b) x = 0.10, (c) x = 0.15 and (d) x = 0.20. Representative acquisition conditions: 15.0 kV accelerating voltage, 8.5 mm working distance and 10 µm scale bar.

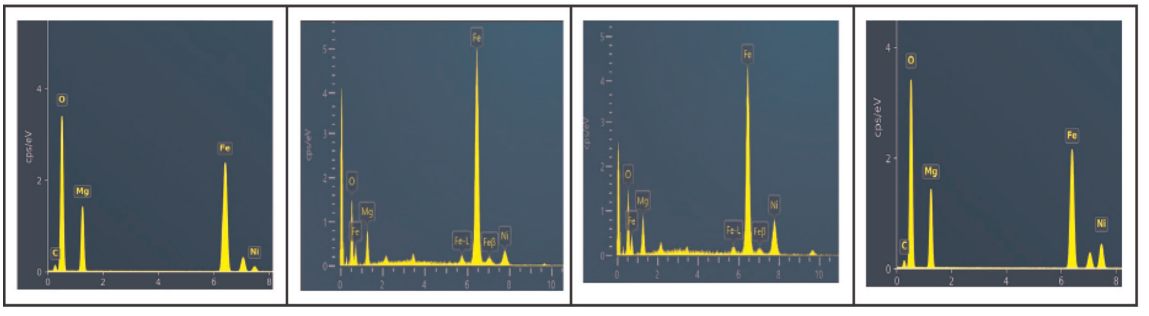


Figure 5 EDS spectra of nominal MFNO: (a) x = 0.05, (b) x = 0.10, (c) x = 0.15 and (d) x = 0.20, showing Mg, Fe, Ni and O signals with a minor C contribution.

micrographs characterize agglomerate morphology rather than the nanoscale crystallite size; the latter being inferred from the XRD line broadening.

EDS spectra (Figure 5) show Mg, Fe, O and Ni signals across the nominal series, supporting incorporation of the intended constituent elements. A small carbon signal is also visible in the spectra and may originate from the mounting medium and/or residual carbonaceous species. EDS is treated here as qualitative elemental confirmation: without quantified standards, oxidation-state analysis or site-sensitive spectroscopy, it does not establish exact stoichiometry, charge-compensation mechanism or crystallographic cation distribution.

Dielectric Response and Loss

Figure 6 compares the measured permittivity for the four compositions, at 100 Hz, 1 kHz, 10 kHz and 100 kHz. At a given temperature, the permittivity decreases with increasing frequency due to the reduced contribution of slow polarization mechanisms. Interfacial/space-charge polarization associated with the Maxwell-Wagner/Koops model for heterogeneous ferrites is often manifested as a low-frequency dispersion, which governs the permittivity at lower frequencies, whereas faster dipolar/electronic processes contribute to the higher-frequency permittivity (Araújo et al., 2021; Chand et al., 2017; Hamdaoui et al., 2019; Senthamilselvan et al., 2024; Tahir et al., 2024). EDS spectra (Figure 5) indicate the presence of Mg, Fe, O and Ni in the nominal series, confirming the inclusion of the desired species in all samples. Some carbon contamination is also observed, which may be related to either the mounting medium or carbonaceous impurities. The EDS analysis was used here for qualitative analysis only. Given the lack of quantitative standards, oxidation state analysis or site-specific spectroscopy, EDS cannot determine stoichiometry, charge compensation mechanism, or crystal chemical ordering.

AC Conductivity

The representative AC-conductivity curves plotted as $\log_{10}\sigma_{ac}$ against 1000/T are shown in Figure 7. For every composition, higher frequency produces higher apparent conductivity, as expected when the field assists localized charge hopping over shorter time scales. At 1 kHz the reported curves span minima of approximately −8.77 to −8.24 and maxima of −6.59 to −6.36 in $\log_{10}\sigma_{ac}$ ($S.cm^{-1}$), depending on composition (Table 3). On moving from high 1000/T toward lower 1000/T (increasing temperature), conductivity rises strongly after the broad minimum, consistent with thermally assisted transport.

Table 3 Representative 1 kHz dielectric/electrical parameters and selected relaxation-fit results.

x	ε′ 33.4°C	ε′ min	Tmin (°C)	ε′ 400°C	ε″ max	Tε″ (°C)	tanδ max	$T_{tan\delta}$ (°C)	$Log_{10}\sigma_{ac}$ min	$Log_{10}\sigma_{ac}$ max	Ea (eV)	R^2
0.05	111.420	9.340	80	183.790	673.4	390	4.590	350	-8.772	-6.426	0.779	0.987
0.10	91.132	22.920	60	202.713	790.6	375	5.015	350	-8.360	-6.357	0.484	0.970
0.15	53.339	11.749	50	186.379	690.9	390	4.654	350	-8.578	-6.415	0.480	0.964
0.20	14.326	14.326	33.4	174.961	465.4	280	4.792	280	-8.236	-6.587	0.662	0.849

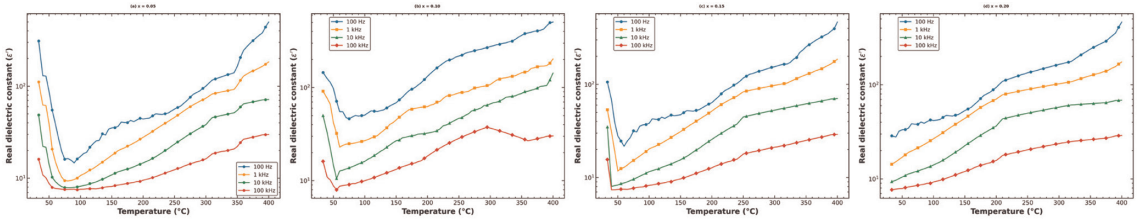


Figure 6 Temperature-dependent ε′ at 100 Hz, 1 kHz, 10 kHz and 100 kHz for (a) x = 0.05, (b) x = 0.10, (c) x = 0.15 and (d) x = 0.20.

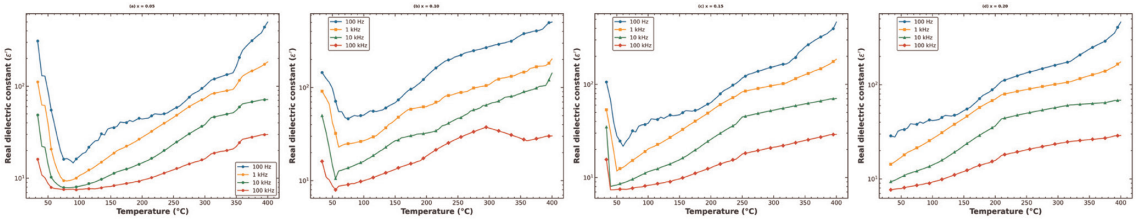


Figure 7 AC conductivity, $\log_{10}\sigma_{ac}$ versus 1000/T at representative frequencies for (a) x = 0.05, (b) x = 0.10, (c) x = 0.15 and (d) x = 0.20.

The low-temperature side of the curves is non-monotonic and should not be fitted with a single Arrhenius conduction law over the whole range. In ferrites, low-frequency interfacial polarization, electrode/contact effects, adsorbed species and multiple hopping processes can all contribute to such behavior. A rigorous assignment of grain and grain-boundary conduction would require impedance-plane analysis or equivalent-circuit fitting, which was not part of the present dataset. Accordingly, the conductivity data are used to demonstrate frequency/temperature tunability rather than to claim a unique microscopic transport model.

Electric Modulus and Dielectric Relaxation

The electric-modulus formalism reduces the dominance of large permittivity contributions and is useful for highlighting relaxation dynamics. Figure 8 shows broad M″ maxima whose position depends on frequency and composition. The maxima are not ideal narrow Debye peaks; broadening and, in some curves, shoulders or multiple features indicate a distribution of relaxation times. Such non-Debye behavior is frequently observed in compositionally and microstructurally inhomogeneous ferrites, in which the contributions from various hopping sites take place in a broad range of time intervals on the expense of others (Hamdaoui et al., 2019; Kumar et al., 2014; Singh et al., 2026).

Table 4 Selected M″ relaxation maxima used for the Arrhenius analysis.

X	Frequency (Hz)	M″ peak temperature (°C)	M″ at selected peak
0.05	100	90	0.032372
0.05	1000	120	0.035425
0.05	10000	180	0.034679
0.05	100000	220	0.038391
0.10	100	90	0.009994
0.10	1000	120	0.013095
0.10	10000	205	0.014119
0.10	100000	360	0.018525
0.15	100	60	0.018785
0.15	1000	130	0.016442
0.15	10000	160	0.020811
0.15	100000	305	0.022038
0.20	100	60	0.013457
0.20	1000	70	0.022105
0.20	10000	90	0.026723
0.20	100000	180	0.029179

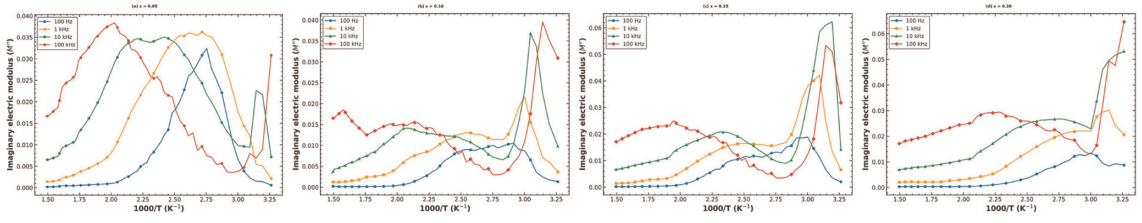


Figure 8 M″ versus 1000/T at representative frequencies for (a) x = 0.05, (b) x = 0.10, (c) x = 0.15 and (d) x = 0.20.

For the Arrhenius analysis, one reproducible higher-temperature M″ feature was selected at each representative frequency. The selected peak temperatures shift to higher temperature with increasing frequency for all compositions, which is the expected signature of thermally activated relaxation. For example, x = 0.05 shifts from 90 °C at 100 Hz to 220 °C at 100 kHz, whereas x = 0.10 shifts from 90 to 360 °C. The detailed peak set is given in Table 4.

Arrhenius Relaxation Analysis

The Arrhenius plot of $\log_{10}\tau$ versus 1000/T (Figure 9) gives effective activation energies of 0.779 eV (x = 0.05), 0.484 eV (x = 0.10), 0.480 eV (x = 0.15) and 0.662 eV (x = 0.20), with corresponding R^2 values of 0.987, 0.970, 0.964 and 0.849, respectively. The decrease in E_a from x = 0.05 to x = 0.10–0.15 indicates that the selected relaxation process becomes thermally more accessible with increasing nominal Ni incorporation. In Mg-Ni ferrites, electrical polarization and charge transport are influenced by cation distribution, localized charge states and hopping pathways within the spinel lattice. Previous studies have shown that changes in Mg/Ni cation distribution can modify the electrical response and related activation behavior (Mittal et al., 2004; Tadi et al., 2010; Revathi et al., 2024). Therefore, the reduction in E_a up to x = 0.15 may be associated with composition-dependent modification of the local cation/defect environment and the corresponding relaxation pathways. The subsequent increase to 0.662 eV at x = 0.20 suggests a change in the effective relaxation landscape rather than a simple monotonic doping dependence. This behavior may arise from changes in local cation arrangement, defect compensation, grain/grain-boundary contributions, or overlapping relaxation processes. However, because the present XRD and EDS measurements do not establish the Ni oxidation state or crystallographic site occupancy, the microscopic origin of the non-monotonic behavior cannot be assigned uniquely. The lower R^2 value of 0.849 for x = 0.20 also indicates greater uncertainty in describing this composition with a single Arrhenius branch.

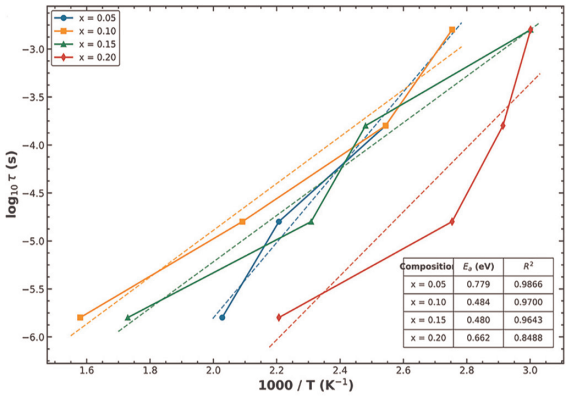


Figure 9 Arrhenius plot of $\log_{10}\tau$ versus 1000/T obtained from selected M″ maxima for MFNO. Linear-fit activation energies and R^2 values are indicated in the figure; the inset labels the composition, E_a (eV), and R^2; the x = 0.20 fit is interpreted as an effective activation energy because of its lower linearity.

The x = 0.20 fit is subject to a particular level of caution due to its significantly lower R^2 than other compositions. Therefore, its 0.662 eV value is reported as an effective activation energy for the chosen branch, not a certain single-barrier material constant. It is better to prefer a conservative interpretation to the selection of different peaks for the improvement of linearity. More dense modulus spectra sampling, impedance spectroscopy and site-sensitive measurements would be helpful for future work to separate overlapping relaxation contributions and charge-compensation mechanisms.

CONCLUSIONS

A nominal MFNO (x = 0.05–0.20) series was synthesized by rapid Tinospora cordifolia-assisted microwave combustion at 600 W, without a separate post-combustion powder calcination step. XRD patterns were characteristic of a dominant cubic spinel phase with nanoscale crystallites. Three line-profile methods independently confirmed a crystallite-size minimum in the vicinity of x = 0.15, while the lattice parameter showed only minor trends across the series. SEM showed porous agglomerated combustion-derived morphologies and EDS qualitatively confirmed Mg, Fe, Ni and O. Sintered pellets showed a pronounced reduction in low-temperature dielectric constant at 1 kHz with increasing nominal Ni content, but high-temperature permittivity was still significant and non-monotonic. Conductivity increased with frequency and exhibited a thermally activated high-temperature rise. Broad frequency-dependent M″ maxima demonstrated distributed non-Debye relaxation. Selected-peak

Arrhenius analysis gave effective activation energies of 0.779, 0.484, 0.480 and 0.662 eV from x = 0.05 to 0.20; the x = 0.20 value is subject to greater uncertainty due to the weaker linear fit. In general, the study has identified a useful structure-dielectric correlation in low-Ni nominal MFNO, and demonstrated that a plant-assisted microwave approach can be used to tune ferrite electrical characteristics with little post-combustion powder processing time. Site occupancy and charge-compensation mechanisms should be addressed in future work using XPS, Mössbauer spectroscopy and/or Rietveld refinement.

Acknowledgment

The authors acknowledge the characterization facilities used for the structural, spectroscopic, microscopic and electrical measurements reported in this work.

Declarations

Conflict of interest: The authors declare that they have no known competing financial interests or personal relationships that could have appeared to influence the work reported in this paper.

REFERENCES

Ali, S. S. L., Selvaraj, S., Batoo, K. M., Chauhan, A., Rana, G., Kalaichelvan, S., & Radhakrishnan, A. (2024). Green synthesis of cubic spinel ferrites and their potential biomedical applications. *Ceramics International, 50,* 52159–52189. https://doi.org/10.1016/j.ceramint.2024.10.084

Araújo, J. C. R., Araujo-Barbosa, S., Souza, A. L. R., Iglesias, C. A. M., Xavier, J., Souza, P. B., Plá Cid, C. C., Azevedo, S., da Silva, R. B., Correa, M. A., de Medeiros, S. N., Silva, E. F., & Bohn, F. (2021). Tuning structural, magnetic, electrical, and dielectric properties of $MgFe_2O_4$ synthesized by sol-gel followed by heat treatment. *Journal of Physics and Chemistry of Solids, 154,* 110051. https://doi.org/10.1016/j.jpcs.2021.110051

Batoo, K. M., Kumar, G., Yang, Y., Al-Douri, Y., Singh, M., Jotania, R. B., & Imran, A. (2017). Structural, morphological and electrical properties of Cd^{2+} doped $MgFe_{2-x}O_4$ ferrite nanoparticles. *Journal of Alloys and Compounds, 726,* 179–186. https://doi.org/10.1016/j.jallcom.2017.07.237

Bouzidi, S., Dhahri, J., Kchaw, M., Essid, M., Juraszek, J., Bouazizi, A., Khirouni, K., & Gassoumi, M. (2025). Tailoring magnetic and dielectric properties of Mg-Ni ferrites via low-concentration Ho^{3+} doping. *Ceramics International, 51,* 41171–41180. https://doi.org/10.1016/j.ceramint.2025.06.340

Chand, P., Vaish, S., & Kumar, P. (2017). Structural, optical and dielectric properties of transition metal (MFe_2O_4; M = Co, Ni and Zn) nanoferrites. *Physica B: Condensed Matter, 524,* 53–63. https://doi.org/10.1016/j.physb.2017.08.060

Dhahri, J., Omri, A., Dhaou, H., Dhahri, E., Graça, M. P. F., Brito, M. E. C., Fausto, R., Pina, J., & Costa, M. M. (2025). Structural, optical, and dielectric studies on transition metals doping (Cu, Ni) in $MgFe_2O_4$ ferrites. *Ceramics International, 51,* 53354–53368. https://doi.org/10.1016/j.ceramint.2025.09.084

Dippong, T., Levei, E. A., & Cadar, O. (2021). Recent advances in synthesis and applications of MFe_2O_4 (M = Co, Cu, Mn, Ni, Zn) nanoparticles. *Nanomaterials, 11,* 1560. https://doi.org/10.3390/nano11061560

Hamdaoui, N., Azizian-Kalandaragh, Y., Khlifi, M., & Beji, L. (2019). Structural, magnetic and dielectric properties of $Ni_{0.6}Mg_{0.4}Fe_2O_4$ ferromagnetic ferrite prepared by sol-gel method. *Ceramics International, 45,* 16458–16465. https://doi.org/10.1016/j.ceramint.2019.05.177

Kumar, G., Shah, J., Kotnala, R. K., Dhiman, P., Rani, R., Singh, V. P., Garg, G., Shirsath, S. E., Batoo, K. M., & Singh, M. (2014). Self-ignited synthesis of Mg-Gd-Mn nanoferrites and impact of cation distribution on the dielectric properties. *Ceramics International, 40,* 14509–14516. https://doi.org/10.1016/j.ceramint.2014.07.017

Manna, A., Pramanik, S., Tripathy, A., Moradi, A., Radzi, Z., Pingguan-Murphy, B., Hasnan, N., & Abu Osman, N. A. (2016). Development of biocompatible hydroxyapatite–poly(ethylene glycol) core–shell nanoparticles as an improved drug carrier: structural and electrical characterizations. *RSC Advances, 6,* 102853–102868. https://doi.org/10.1039/C6RA21210G

Mittal, V. K., Bera, S., Nithya, R., Srinivasan, M. P., Velmurugan, S., & Narasimhan, S. V. (2004). Solid state synthesis of Mg-Ni ferrite and characterization by XRD and XPS. *Journal of Nuclear Materials, 335,* 302–310. https://doi.org/10.1016/j.jnucmat.2004.05.010

Pramanik, S., Hanif, A. S. M., Pingguan-Murphy, B., & Abu Osman, N. A. (2013). Morphological change of heat treated bovine bone: a comparative study. *Materials, 6,* 65–75. https://doi.org/10.3390/ma6010065

Revathi, R., Sukumar, M., Kumar, A., Gupta, M., Udhaya, P. A., Sehgal, S. S., Pandit, B., Sundararajan, M., Subramani, A., Dash, C. S., Senthilkumar, N., & Ubaidullah, M. (2024). Facile synthesis of Ni^{2+} doped $MgFe_2O_4$ spinel nanoparticles: Structural, optical, magnetic, and dielectric behavior. *Journal of Inorganic and Organometallic Polymers and Materials, 34,* 374–386. https://doi.org/10.1007/s10904-023-02820-8

Senthamilselvan, T., Nithiyanantham, S., Kogulakrishnan, K., Mahalakshmi, S., Lakshmigandhan, T., Mohan, R., & Gunasekaran, B. (2024). Structural, magnetic, electric and electrochemical studies on zinc doped magnesium ferrite nanoparticles - sol-gel method. *Heliyon, 10,* e25511. https://doi.org/10.1016/j.heliyon.2024.e25511

Sickafus, K. E., Wills, J. M., & Grimes, N. W. (1999). Structure of spinel. *Journal of the American Ceramic Society, 82,* 3279–3292. https://doi.org/10.1111/j.1151-2916.1999.tb02241.x

Singh, D. P., Akanksha, Dhariwal, N., Yadav, P., & Kumar, V. (2026). Magnetic and temperature-assisted dielectric dynamics in Ni^{2+}/Co^{2+} dual-cation substituted $MgFe_2O_4$ semiconducting ferrites: Insights into composition-property tunability. *Ceramics International.* Advance online publication. https://doi.org/10.1016/j.ceramint.2026.02.259

Srimathi, R., Rao, N. V. S. S. S., Merlin, A., Kiruthika, R., Selvaraj, A., Abdelkader, O. H., Dash, C. S., Revathi, S., Ahamed, A., Rajabathar, J. R., Sundararajan, M., Yuvaraj, S., & Rajadurai, L. (2025). Investigation of structural, magnetic, optical and dielectric characteristics of Al-doped $MgFe_2O_4$ nanoparticles. *Solid State Sciences, 159,* 107761. https://doi.org/10.1016/j.solidstatesciences.2024.107761

Srinivasan, T. T., Srivastava, C. M., Venkataramani, N., & Patni, M. J. (1984). Infrared absorption in spinel ferrites. *Bulletin of Materials Science, 6,* 1063–1067.

Suresh Kumar, G., Srinivasan, R., Karunakaran, G., Kolesnikov, E., Kim, M., & Karpenkov, D. Y. (2021). Microwave-assisted combustion synthesis of soft ferromagnetic spinel MFe_2O_4 (M = Ni, Mg, Zn) nanoparticles using Citrus limon fruit extract as a fuel. *Applied Physics A,* 127, 546. https://doi.org/10.1007/s00339-021-04694-4

Tadi, R., Kim, Y., Sarella, A. K., Kim, C. G., & Ryu, K. S. (2010). Relation of structure and magnetic properties in nickel substituted $MgFe_2O_4$. *Journal of Magnetism and Magnetic Materials, 322,* 3372–3376. https://doi.org/10.1016/j.jmmm.2010.06.029

Tahir, M., Imran, M., Shah, Z. H., Riaz, M. B., Riaz, S., & Naseem, S. (2024). Phase formation and dielectric properties of $MgFe_2O_4$ nanoparticles synthesized by hydrothermal technique. *Heliyon, 10,* e29553. https://doi.org/10.1016/j.heliyon.2024.e29553

Udayabhanu, Nethravathi, P. C., Pavan Kumar, M. A., Suresh, D., Lingaraju, K., Rajanaika, H., Nagabhushana, H., & Sharma, S. C. (2015). Tinospora cordifolia mediated facile green synthesis of cupric oxide nanoparticles and their photocatalytic, antioxidant and antibacterial properties. *Materials Science in Semiconductor Processing, 33,* 81–88. https://doi.org/10.1016/j.mssp.2015.01.034

Vishnu, G., Singh, S., Kaul, N., Ramamurthy, P. C., Naik, T. S. S. K., Viswanath, R., Kumar, V., Naik, H. S. B., Prathap, A., Anil Kumara, H. A., Singh, J., & Khan, N. A. (2023). Green synthesis of nickel-doped magnesium ferrite nanoparticles via combustion for facile microwave-assisted optical and photocatalytic applications. *Environmental Research, 235,* 116598. https://doi.org/10.1016/j.envres.2023.116598